Aggregate

WILEY

Aggregate Open Access

RESEARCH ARTICLE OPEN ACCESS

A Molecular Descriptor Guided Asymmetric Strategy for High Carrier-Mobility Light-Emitting Organic Semiconductors

Jie Liu[1] | Qi Sun[2] | Yanjun Shi[3] | Tong Jiang[2] | Xiaosong Shi[1] | Jiali Liu[4] | Jing Zhang[1] | Yaxin Zhai[4] | Yu Wang[5] | Qian Peng[6] | Wenping Hu[7] | Yunqi Liu[1] | Zhigang Shuai[2] | Lang Jiang[5]

[1]Beijing National Laboratory for Molecular Sciences, Key Laboratory of Organic Solids, Institute of Chemistry, Chinese Academy of Sciences, Beijing, China | [2]MOE Key Laboratory of Organic OptoElectronics and Molecular Engineering, Department of Chemistry, Tsinghua University, Beijing, China | [3]Jiangsu Key Laboratory of Advanced Materials and Technology, School of Petrochemical Engineering, Changzhou University, Changzhou, China | [4]Key Laboratory of Low-Dimensional Quantum Structures and Quantum Control of Ministry of Education, Department of Physics, Hunan Normal University, Changsha, China | [5]School of Chemical Engineering and Technology, Hebei University of Technology, Tianjin, China | [6]University of Chinese Academy of Sciences, Beijing, China | [7]Tianjin Key Laboratory of Molecular Optoelectronic Sciences, Department of Chemistry, School of Sciences, Tianjin University, Tianjin, China

Correspondence: Qian Peng (qianpeng@ucas.ac.cn) | Zhigang Shuai (zgshuai@tsinghua.edu.cn) | Lang Jiang (ljiang@hebut.edu.cn)

Received: 20 October 2025 | **Revised:** 15 November 2025 | **Accepted:** 18 November 2025

Keywords: aggregated states | asymmetric strategy | carrier mobility | molecular descriptor | photoluminescence quantum yield (PLQY)

ABSTRACT

Combining high mobility and high-efficiency luminescence in one material is challenging because of their contradictory design principles. Here, under the three-state exciton model, a molecular descriptor $O = (|t_h + t_e| - |t_h - t_e|)/2J$ is proposed to quantitatively design materials with balanced luminescence and mobility in aggregated states, where a large O would promise high crystalline photoluminescence quantum yield (PLQY) with small J (excitonic coupling) and significant t_h and t_e (hole and electron transfer integrals) would indicate high mobility. Through theoretical calculation and experimental validation, it is found that the asymmetric anthracene derivatives are quite effective in simultaneously achieving high mobility and high PLQY. Following the asymmetric guideline, the newly developed compounds, 2-phenyl vinyl anthracene (2-PhVA) and 6-(2-(anthracene-2-yl)vinyl)benzo[b]thiophene (6-BTVA) demonstrate high O values alongside excellent performance: 2-PhVA exhibits a PLQY of 81.5% and a maximum hole mobility of 10.0 $cm^2\ V^{-1}\ s^{-1}$, and 6-BTVA shows a PLQY of 30.9% with a maximum mobility of 9.3 $cm^2\ V^{-1}\ s^{-1}$. The above results demonstrate the validation of the descriptor and the asymmetric strategy in further developing high-mobility light-emitting aggregated materials.

1 | Introduction

Semiconductor materials combined with high mobility and high photoluminescence quantum yield (PLQY) in aggregated states have attracted widespread research interest. These materials not only provide the foundation for the integration of organic field-effect transistors (OFETs) and organic light-emitting diodes (OLEDs), but also establish the material basis for achieving electrically pumped organic lasers [1–8]. Although coplanar π-conjugated materials with dense packing are ideal for high-performance OFETs [9], they often suffer from aggregation-caused quenching (ACQ), which lowers their PLQY. Conversely, the high-PLQY materials used in OLEDs typically exhibit poor charge carrier mobility [10, 11]. After years of unremitting efforts, a delicate balance has been achieved, and a series of high-mobility light-emitting materials in aggregated states has been developed

[12–20]. Among these materials, anthracene derivatives, especially 2,6-diaryl-substituted materials, have attracted intensive research interest [21–32], which provides the molecular model for theoretical study. In theoretical calculations, a three-state exciton model has been proposed to explain the luminescence behaviors in anthracene derivatives: [33, 34] when $t_h \approx t_e = t$ and $|t| > \sqrt{2}|J|$, where t is the transfer integral and J is the excitonic coupling. Materials with eclipsed packing are more conducive to achieving high mobility and high PLQY simultaneously. Model case studies have also been conducted under the perturbative and resonance regimes [35, 36]. However, breaking the existing bottleneck of designing such materials from the close combination of theoretical calculation and experimental validation is still challenging. Furthermore, compared with the intensively studied symmetrically substituted anthracene derivatives [22, 24, 26–30, 37], the asymmetric anthracene derivatives are less studied [21, 23, 25, 38], yet very few examples of asymmetric anthracene derivatives were found with efficient PLQY and charge transport properties. For example, the asymmetric 2-(2-naphthyl) anthracene (NaAnt) [23] showed mobility of 1.1 $cm^2 V^{-1} s^{-1}$ in thin-film OFETs and superior PLQY (Φ = 40.3%) than its symmetric counterparts 2,6-di-(2-naphthyl) anthracene (dNaAnt) [26] (Φ = 29.2%). Thus, the asymmetric substitution might be a promising strategy for constructing high-mobility emissive anthracene derivatives, which promotes our interest in the systematic theoretical and experimental study of asymmetric materials.

In this study, first, by comprehensively considering the relationship between $t_{e(h)}$ and J, we proposed a molecular descriptor O ($O = (|t_h + t_e| - |t_h - t_e|)/2J$), where larger O indicates higher crystalline PLQY. The validity of descriptor O is confirmed by taking the asymmetric 2-phenyl vinyl anthracene (2-PhVA) and the symmetric 2,6-di-2-phenylvinyl anthracene (DPVAnt) as an example. The asymmetric 2-PhVA predicted with smaller J and larger O values was confirmed with a high PLQY of (81.5 ± 5.52)% in experiments, while a PLQY of (8.0 ± 1.05)% was obtained for symmetric DPVAnt with a smaller O value. Under the asymmetric substitution guideline, a series of benzothiophene (BT)-substituted asymmetric anthracene derivatives has been developed. Theoretically calculated weak J, small reorganization energy (λ), and large t indicate their potential in high-mobility emissive semiconductors. Further experiment results suggest that 6-(2-(anthracene-2-yl)vinyl)benzo[b]thiophene (6-BTVA) with the larger O value and eclipsed stacking exhibits higher crystalline PLQY (30.9 ± 0.53)% and mobility (9.3 $cm^2 V^{-1} s^{-1}$) than materials with smaller O value and staggered stacking.

2 | Results and Discussion

Under the three-state exciton model (Figure 1a), there are two kinds of excitons in H-type aggregates: the Frenkel excitons (FE) and the charge transfer exciton (CTE), and the CTE effectively couples with bright FE (FE_S) to generate the transition dipole-allowed lowest-lying excited state under the condition of $t_h \approx t_e = t$ and $|t| > \sqrt{2}|J|$, as seen in Figure 1a. More importantly, materials with eclipsed stacking are more prone to show high performance than those with staggered packing (Figure 1b) [34].

The coupling between the CTE and bright FE (FE_S) and dark FE (FE_{AS}) is $t_h + t_e$ and $t_h - t_e$, respectively. Here, we assume the energy zero point is the excitation energy of the S_1 state in the monomer and the energy of the CTE is E_{CT}, three-state model Hamiltonian which in the basis of $\{|FE_{AS}\rangle; |FE_S\rangle; |CTE\rangle\}$ reads:

$$\hat{H} = \begin{bmatrix} -J & 0 & t_h - t_e \\ 0 & J & t_h + t_e \\ t_h - t_e & t_h + t_e & E_{CT} \end{bmatrix} \quad (1)$$

On the one hand, the CTE may play a role in the final luminescence behavior only if the t_h and t_e are larger than J. On the other hand, $t_h + t_e$ must be larger enough than $t_h - t_e$ to induce an electronic transition dipole (μ) allowed S_1 state. Since dark FE and CTE are both electronic transition dipole forbidden states, the electronic transition dipole of the S_1 state is only derived from the bright FE. Hence, we put forward the descriptor O, which is proportional to the coupling difference between the CTE with bright FE and dark FE ($|t_h + t_e| - |t_h - t_e|$), and inversely proportional with J:

$$O = \frac{|t_h + t_e| - |t_h - t_e|}{2J} \quad (2)$$

In this framework, O reflects the competition between the coupling of the CTE with the bright and dark FE states. The CTE couples to the bright state through ($t_h + t_e$) and to the dark state through ($t_h - t_e$). When $J < 0$, the dark state lies below the bright state, and efficient luminescence requires that the coupling with the bright state ($t_h + t_e$) becomes sufficiently large to overcome both ($t_h - t_e$) and J, allowing the bright state to become the lowest-energy emissive state. In the eclipsed packing mode, t_e and t_h usually have the same sign, leading to a large ($t_h + t_e$) term that favors radiative recombination. In contrast, in the staggered packing mode, t_e and t_h often have opposite signs, reducing ($t_h + t_e$) and thus suppressing emission. Therefore, the eclipsed packing mode is generally more favorable for achieving both efficient charge transport and strong luminescence.

Here, we consider the value of J and $t_h + t_e$ are 10 meV and 40 meV, respectively, to give an explicit parameter study of the impact of the relationship between O (0~2) and luminescence behavior, since direct diagonalization of all the symbols would give tediously complicated results. Once the diagonalization of Equation 1 is applied, we could get the contribution of the bright FE in the lowest eigenstate, which could represent the change of the oscillator strength from monomer to dimer ($f_{dimer}/f_{monomer}$). The relation between $f_{dimer}/f_{monomer}$ and O, along with the different E_{CT} is plotted in Figure 1c. It can be seen that $f_{dimer}/f_{monomer}$ is increasing with the enhancement of O, and its maximum appears at O = 2.0 with $t_h - t_e = 0$. Along with the increase of E_{CT}, $f_{dimer}/f_{monomer}$ is generally enhanced with more contribution of the lower energy bright FE. That is, large t_h and t_e with the same sign and comparable value, and small J would promise large O and high PLQY. Under the dipole–dipole approximation, J can be calculated as:

$$J = \frac{\vec{\mu_1} \cdot \vec{\mu_2} - 3\left(\vec{\mu_1} \cdot \hat{e}\right)\left(\vec{\mu_2} \cdot \hat{e}\right)}{4\pi\varepsilon R^3} \quad (3)$$

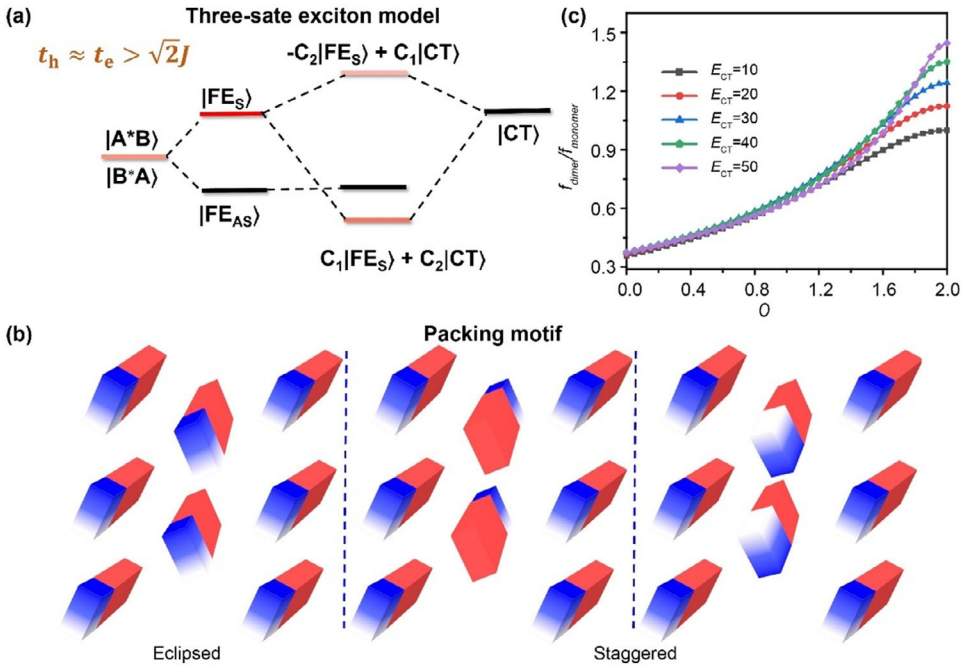

FIGURE 1 | (a) Schematic three-state exciton model of CT-induced luminescence in H-type aggregates. The saturation of the red color denotes the strength of the transition dipole moment, and the black color corresponds to transition-dipole forbidden dark states. (b) Different packing motifs in the crystals, different colors present different molecular fragments and orientations. Eclipsed stacking occurs when adjacent molecules align in the same orientation, while staggered stacking involves neighboring molecules adopting opposite orientations. (c) The relation between O and $f_{\text{dimer}}/f_{\text{monomer}}$ along with different ECT (Unit: meV).

$\vec{\mu}_1$ and $\vec{\mu}_2$ are the transition dipole moment of the two monomers, R is the distance between the centers of the dipoles, $\hat{e}$ is the unit vector in the direction of R, ε is the dielectric constant. If two monomers are identical, $J \propto \mu^2$. The longer the conjugation length of a molecule, the larger the transition dipole moment will be. Combining Equations (2) and (3), it is predicted that molecules with asymmetric aryl substitutions possess shorter π-conjugation length, which would induce smaller J and larger O and potentially higher crystalline PLQYs. In-depth validation of O toward high PLQY among the symmetric and asymmetric anthracene derivatives was carried out.

The symmetrically and asymmetrically substituted anthracene derivatives DPVAnt and 2-PhVA with high charge mobility are chosen as examples [37, 38]. High-quality single crystals of DPVAnt and 2-PhVA were prepared via the physical vapor transport (PVT) method [39] (see details in Experimental Section 4). Their photophysical properties, including absorption and emission spectra, time-resolved fluorescence, and PLQY in solution and crystalline phase, are recorded and summarized in Figure 2, Table 1, and Table S1 [40]. As shown in Figure 2, the absorption and emission spectra of both compounds exhibit well-structured vibrational peaks, which indicate that they are very rigid conjugated systems. Compared to the spectra in the solution, the absorption and emission spectra are red-shifted in the crystalline phase for the two compounds (Figure 2a,b). It is found that the PLQY of 2-PhVA is enhanced from 49.0% in solution to (81.5 ± 5.52)% in crystal, behaving crystalline-enhanced emission [41], in comparison, that of DPVAnt is decreased from 84% in solution to (8.0 ± 1.05)% in crystal, indicating crystalline-quenched emission. Time-resolved photoluminescence spectroscopy was conducted for monomer and crystalline samples, from which lifetimes of 8.8 and 7.7 ns, 3.3 and 4.2 ns were extracted for monomers and crystals of 2-PhVA and DPVAnt (Figure 2c), respectively. Correspondingly, from monomers in solution to aggregated crystals, the radiative decay rate becomes faster for 2-PhVA (from 5.57×10^7 to 1.06×10^8) but slower for DPVAnt (from 2.55×10^8 to 1.90×10^7). On the contrary, the nonradiative decay rate becomes slower for 2-PhVA but faster for DPVAnt. Besides, ultrafast transient absorption (TA) spectroscopy was recorded for their crystal samples, verifying the existence of mixed states between CT and FE (TA Measurement and Figure S1 in Supporting Information) [42, 43], indicating the applicability of the three-state exciton model in these molecular systems.

To reveal the mechanism of similar bathochromic behavior and distinct PLQYs from solution to crystal for 2-PhVA and DPVAnt, we theoretically examine the excited-state electronic structures and properties in solution and crystal, as well as intermolecular J and t, as shown in Table 1 and Figure 2d. As expected, the more extensive conjugation in symmetric DPVAnt generates larger transition dipole moments and smaller reorganization energies compared to asymmetric 2-PhVA, which results in a higher PLQY of DPVAnt than 2-PhVA in solution. In crystals, both compounds adopt favored eclipsed packing motifs, and there are many intermolecular interactions (Figure S2). The calculated largest J between a central molecule and its surrounding molecules are positive values (Figure 2d), which are 31.33 meV and 67.29 meV for 2-PhVA and DPVAnt, respectively, suggesting the molecular packing is mainly face-to-edge H-type aggregates. The enhanced J of DPVAnt over 2-PhVA is deduced from the larger transition dipole moment of DPVAnt than 2-PhVA in terms of dipole–dipole interaction. The calculated values of t_h and t_e are of the

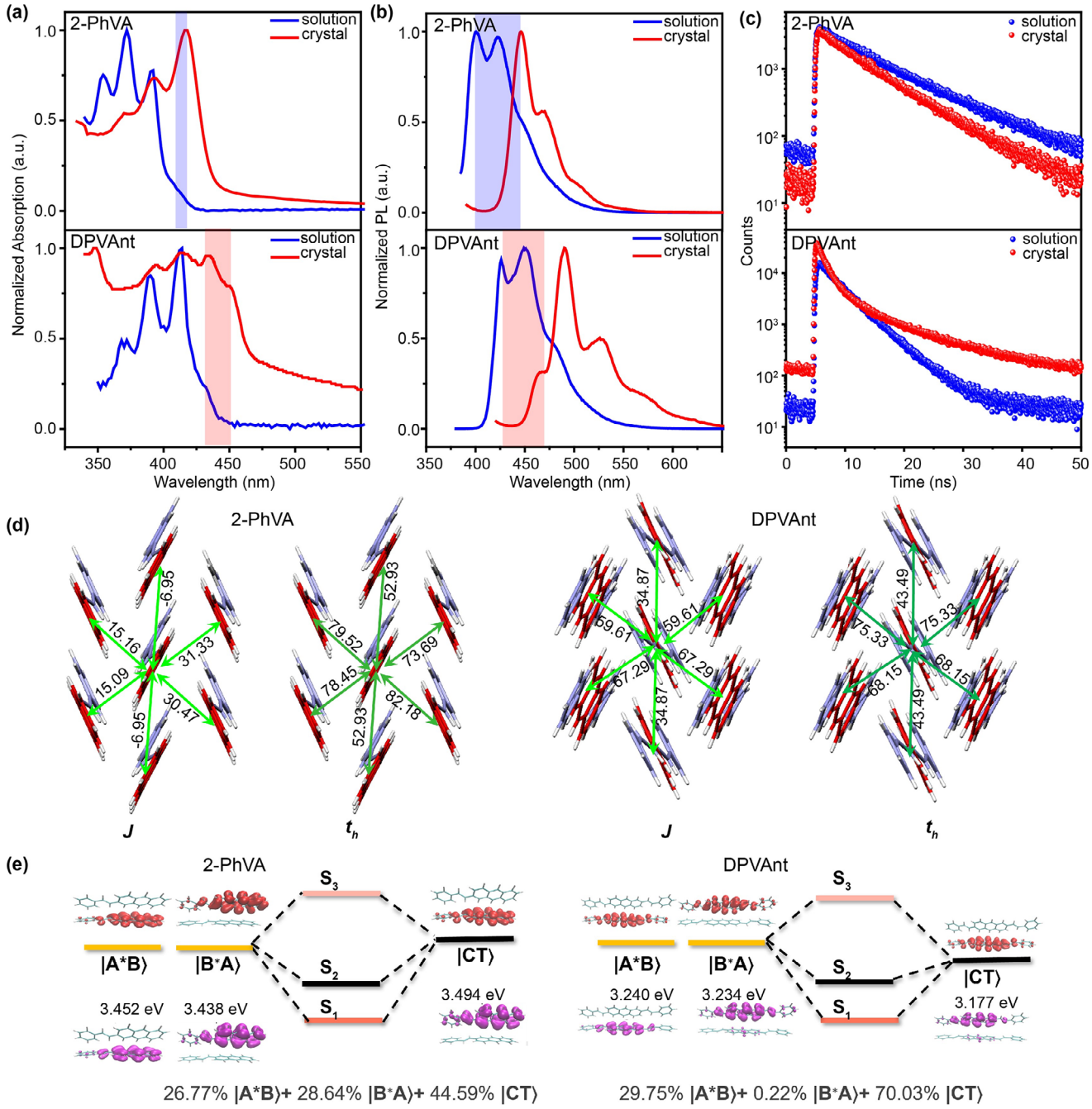

FIGURE 2 | (a) Absorption spectra, (b) photoluminescent spectra, and (c) lifetime test of 2-PhVA and DPVAnt in dilute solution and single crystals. The colored areas (blue for 2-PhVA and pink for DPVAnt) present the bathochromic shifts of the samples from dilute solution to single crystals. (d) Excitonic coupling (J) and hole transfer integral (t_h) in the 2D herringbone lattice of 2-PhVA and DPVAnt. (e) Attachment–detachment densities and excitation energies of the resulting diabatic states of 2-PhVA and DPVAnt. The percentages listed below the excitation energy are the contribution of the corresponding diabatic state to the adiabatic S_1 state.

same sign (Table 1), and the large t_h values (Figure 2d) for the two compounds suggest the occurrence of an intermolecular CT exciton in the two aggregates. To confirm this point, the adiabatic states of the selected dimer are decomposed into the diabatic states, as plotted in Figure 2e. The excited-state energy levels of both compounds obey the three-state exciton model, which not only explains the bathochromic behavior from solution to crystal [33, 44], but also indicates the feasibility of using O to evaluate their photoluminescent properties. Based on the above J and t, O values of 1.78 and 0.36 are obtained for 2-PhVA and DPVAnt, indicating 2-PhVA exhibits higher PLQY than DPVAnt in crystals, which corresponds well with the experiment results. Hence, it can be concluded that, in the eclipsed packing motif, the asymmetric anthracene derivative could outperform its symmetric counterparts in PLQY and strengthen the asymmetric substitution strategy for high-mobility light-emitting anthracene derivatives.

Based on the asymmetric substituent strategy, the BT substituent is then introduced to anthracene, 6-(anthracen-2-yl)benzo[b]

TABLE 1 | Summary of theoretical and experimental details of anthracene derivatives.

Compounds	2-PhVA	DPVAnt	6-BTA	6-BTVA	6-BTEA
k_r(sol.) [s^{-1}]	5.57×10^7	2.55×10^8	5.45×10^7	7.05×10^7	1.18×10^8
k_{nr}(sol.) [s^{-1}]	5.80×10^7	4.85×10^7	1.27×10^8	3.47×10^7	7.80×10^7
PLQY (sol.)[a]	0.49	0.84	0.30	0.67	0.60
k_r(cry.) [s^{-1}]	1.06×10^8	1.90×10^7	3.44×10^7	3.96×10^7	3.93×10^7
k_{nr}(cry.) [s^{-1}]	2.40×10^7	2.19×10^8	3.36×10^8	8.86×10^7	2.05×10^8
PLQY (cry.)[a]	81.5 ± 5.52%	8.0 ± 1.05%	9.3 ± 0.28%	30.9 ± 0.53%	16.1 ± 3.02%
μ [Debye]	8.66	9.5	5.11	11.97	8.67
λ [meV]	187.6	184.3	219.4	192.8	177.1
J [meV]	31.33	67.29	14.3	25.2	39.8
t_h [meV]	73.69	68.15	−13	62.4	−87.6
t_e [meV]	55.82	24.32	52.7	26.5	65.6
O	1.78	0.36	−0.91	1.05	−2.2
Mobility [$cm^2\ V^{-1}\ s^{-1}$][b]	44.0 (10.0)	25.9 (4.3)	2.1 (1.8)	33.5 (9.3)	45.5 (6.5)

[a]Experimental results of PLQY in THF solution and crystal.
[b]The mobilities in parentheses are the experimental values.

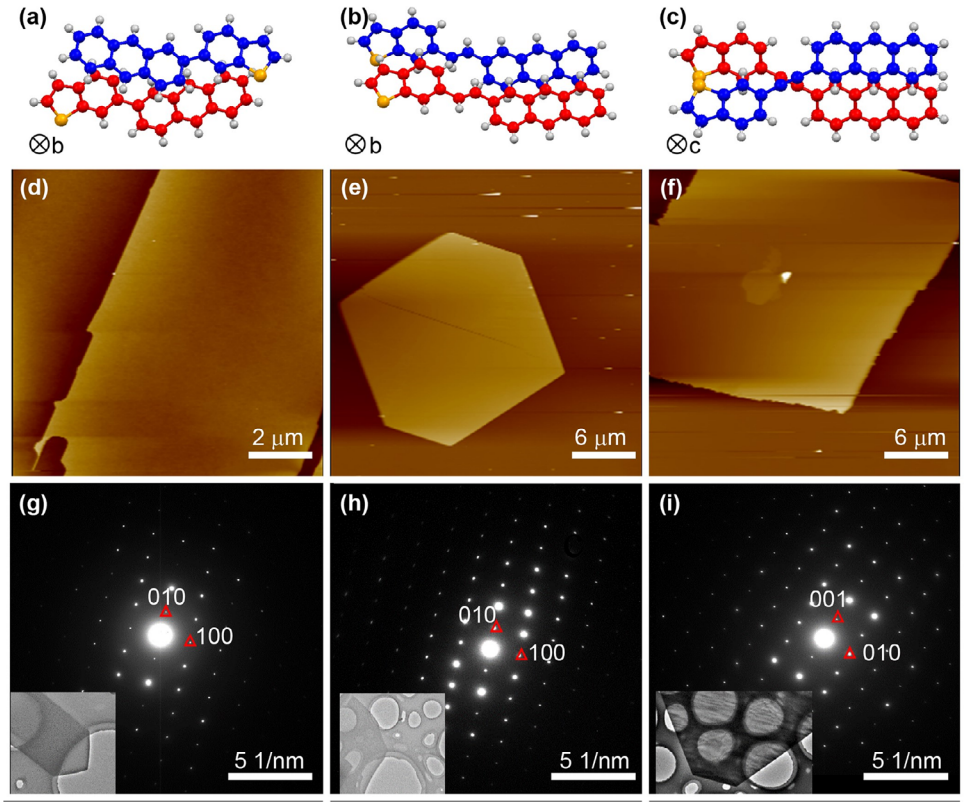

FIGURE 3 | Molecular pairs demonstrating the staggered stacking of (a) 6-BTA and (c) 6-BTEA, and the eclipsed stacking of (b) 6-BTVA in aggregated states. Red and blue represent carbon atoms, light gray represents hydrogen atoms, and orange represents the sulfur atoms. (d), (e), and (f) are typical AFM images, and (g), (h), and (i) are the TEM and corresponding SAED patterns of 6-BTA, 6-BTVA, and 6-BTEA single crystals, respectively.

thiophene (6-BTA), 6-BTVA, and 6-(anthracen-2-ylethynyl)benzo [b]thiophene (6-BTEA) are designed and synthesized (Figure 3, Figure S3, and Supporting Information). High-quality single crystals were grown by slow evaporation of chlorobenzene and analyzed by X-ray diffraction (Table S2). As shown in Figure S4, all three compounds exhibit herringbone packing motifs with multiple short contacts, analogous to 2-PhVA and DPVAnt. This structural similarity indicates their conformity with the

three-state exciton model. Besides, differences also existed among the three compounds. In Figure 3a–c, the herringbone-packed pairs of molecules are demonstrated, and alternated molecular orientations can be observed along the long and short axes for 6-BTA and 6-BTEA molecules, consistent with the staggered stacking motif shown in Figure 1b. While the orientation of the molecular pairs in 6-BTVA is identical (Figure 3b), which is the eclipsed packing, and would favor balanced charge mobility and luminescence as discussed above. Based on the single crystal structure of the three compounds, the decomposition of the S_1 state is performed, and the J, t_h, t_e, and O are calculated and shown in Table 1. As expected, the three compounds consist of locally excited (LE) and CT states (Figure S5), consistent with the three-state exciton model. Moreover, as inferred above, the t_h and t_e are of the opposite sign with negative O value in the staggered stacking 6-BTA and 6-BTEA, which makes the $|CT\rangle$ couple with the transition dipole-forbidden $|FE_{AS}\rangle$, leading to the quenching of fluorescence; while t_h and t_e are of the same sign along with positive O value in the eclipsed packing 6-BTVA, which induces the $|CT\rangle$ couples with the transition dipole-allowed $|FE_S\rangle$, resulting in better luminescence. Regarding transport behavior, the hole mobility values of 2.1 $cm^2 V^{-1} s^{-1}$, 33.5 $cm^2 V^{-1} s^{-1}$, and 45.5 $cm^2 V^{-1} s^{-1}$ obtained by the home-built MOMAP program [45–47] are determined for 6-BTA, 6-BTVA, and 6-BTEA, respectively. Overall, three organic luminescent semiconductors are designed, and 6-BTVA is predicted to possess strong luminescence and high mobility.

To verify the prediction above, the photophysical and charge transport properties of the three compounds are studied. The comprehensive PL parameters are included in Table 1 and Figures S6–S9. In dilute solution, 6-BTVA and 6-BTEA showed slight bathochromic shifts in absorption and higher PLQY compared with 6-BTA (Figure S6, Table 1, and Table S3), which is caused by the enlargement of conjugation and rigidity via vinyl and ethynyl groups. Compared to the solutions, the crystalline samples exhibit a bathochromic shift in their absorption spectra (Figure S7), and the PLQYs are decreased to different extents owing to the generation of FE and CTE. TA measurements for 6-BTA and 6-BTVA (see Figure S8 and TA Measurement in Supporting Information) confirm the mixing of FE and CTE states, supporting the applicability of the three-state model, which is consistent with the behavior of 2-PhVA and DPVAnt. Unfortunately, the TA spectra for 6-BTEA exhibited a poor signal-to-noise ratio and could not be included in this analysis. Among the three compounds, the eclipsed packing 6-BTVA shows the highest PLQY of (30.9 ± 0.53)% in the crystal because of the largest calculated O value. In comparison, PLQY of (9.3 ± 0.28)% and (16.1 ± 3.02)% were obtained for 6-BTA and 6-BTEA. These findings validate the computational prediction that eclipsed stacking architectures exhibit enhanced performance relative to their staggered counterparts.

To compare their charge transport properties, single-crystal OFETs were fabricated on octadecyl trichlorosilane (OTS)-treated Si/SiO_2 (300 nm) substrates (Supporting Information). As the optical microscopy images showed in Figure S10, the two-dimensional molecular interactions yield hexagon- and rhombus-like micro-crystals. Atomic force microscopy (AFM) measurements (Figure 3d–f and Figure S11) reveal smooth morphology and thickness in the range of ~10 to hundreds of nanometers for the crystals. Out-of-plane X-ray diffraction (Figure S12), in-plane transmission electron microscopy (TEM) and corresponding selected area electron diffraction (SAED) patterns are illustrated in Figure 3g–i, and all the data can be well-indexed according to the single crystal file, indicating the same packing motif of the micro-crystals and large crystals.

According to the XRD and TEM results, all three compounds grow with their long molecular axis perpendicular to the substrate (Figure 4a), with their herringbone packing motif perpendicular to the surface normal, which is essential for high charge carrier mobility. Transistors based on single crystals were fabricated by mechanically transferring gold films onto the top of the single crystals [48]. The typical transfer and output curves are shown in Figure 4b–g and Figure S13. All the devices demonstrate typical p-type charge transport behavior. The field-effect mobility (μ_{FET}) was derived using the following relationship in the saturation region:

$$\mu_{FET} = \left(\frac{2L}{WC_i}\right)\left(\frac{d\sqrt{I_{DS}}}{dV_G}\right)^2, \quad (4)$$

where, C_i represents the areal capacitance, W and L are the channel width and length, I_{DS} is the drain current, and V_G is the gate voltage, respectively. To guarantee reliability, mobilities were calculated based on the slope values extracted by fitting a linear relation between $(-I_{DS})^{1/2}$-V_G in the range from 0/−2 V to −60 V [49, 50]. The highest (average) saturated mobilities are 1.8 (0.87), 9.3 (4.76), 6.5 (3.78) $cm^2 V^{-1} s^{-1}$ for 6-BTA, 6-BTVA, and 6-BTEA, respectively. The mobility distributions are illustrated in Figure 4h–j. The output curves reveal obvious contact resistance, which could be attributed to the mismatch between the work function of gold electrodes and the highest occupied molecular orbital (HOMO) levels of organic semiconductors (Figure S14). The contact resistance also induced a degradation of saturated mobility at high V_G and differences between the linear (tested at $V_{DS} = -5$ V, Figure S13) and saturated mobilities. Besides, the contact resistance and possible interfacial/structural defects would all contribute to the variation of the calculated and experimental mobility results. Despite suboptimal OFET performance, this study reveals that the high-mobility, vinyl-bridged eclipsed packing in 6-BTVA, which possesses the largest O value and exhibits the highest crystalline PLQY. This direct correlation motivates further investigation into O as a predictor for luminescent properties.

To further verify the descriptor, we plot the PLQY in the crystalline phase versus O as shown in Figure 5a for the systems in which $t_h * t_e > 0$, namely, 6-BTVA, 2-PhVA [38], DPVAnt [37] in this context and NaAnt [23], dNaAnt [26], DP-BPEA [27], 2,6-DAN [29], (Figure S15) 2,6-DPSAnt [22]. It can be seen in Figure 5a that the calculated O and the experimental PLQY value in the crystal show a good linear relationship with a linear fitting coefficient $R^2 = 0.8879$, verifying the validity of O to represent the luminescence efficiency in crystals. Furthermore, the asymmetric systems exhibit enhanced luminescence and a larger O value compared to the corresponding symmetric ones. This clearly demonstrates the effectiveness of the asymmetric substituent strategy in anthracene derivatives for constructing highly luminescent p-type semiconductors. The obtained 2-PhVA in this work shows the highest PLQY in the crystal among

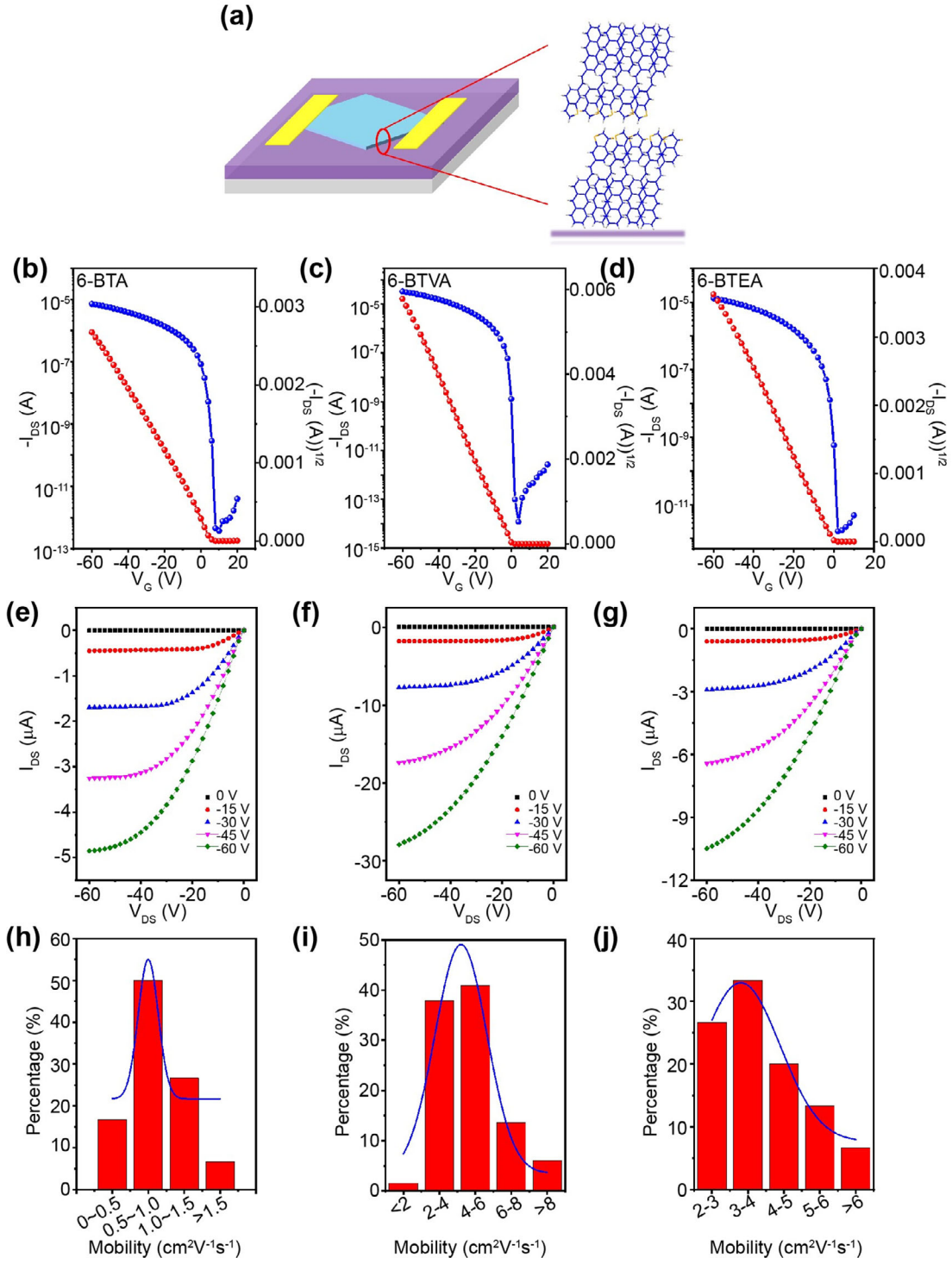

FIGURE 4 | (a) Schematic illustration of the device structure and the molecular orientations. (b), (c), and (d) are typical transfer curves tested at $V_{DS} = -60$ V, (e), (f), and (g) are typical output curves, and (h), (i), and (j) are the mobility distributions of 6-BTA, 6-BTVA, and 6-BTEA single crystal OFETs, respectively. The number of devices used for the statistics is 60, 66, and 60, respectively.

anthracene derivatives with excellent charge transport properties, as illustrated in Figure 5b.

3 | Conclusions

In summary, we introduced a descriptor *O*, based on a three-state exciton model, to predict luminescence efficiency in high-mobility H-aggregates. Asymmetric anthracene derivatives with eclipsed stacking were found to yield higher *O* values and enhanced crystalline PLQYs. This was validated by comparing symmetric DPVAnt ($O = 0.36$, PLQY = 8.0 ± 1.05%) with its asymmetric analog 2-PhVA ($O = 1.78$, PLQY = 81.5±5.52%), where reduced π-conjugation in 2-PhVA lowered exciton coupling below the transfer integral, favoring high luminescence. Further application of this asymmetric strategy led to derivatives of eclipsed

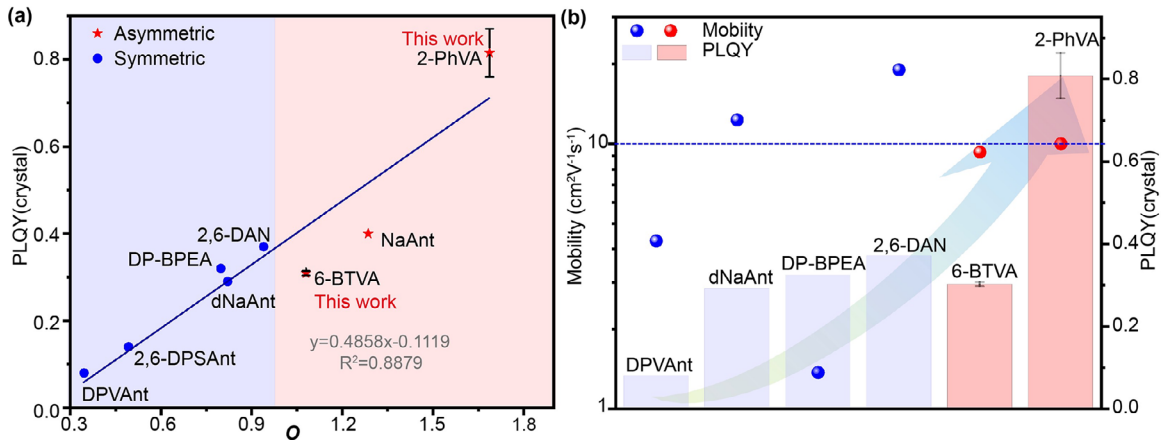

FIGURE 5 | (a) The linear relationship between *O* and PLQY (crystal) for the molecules shown in Figure S15. (b) Comparison of PLQY and single crystal mobility of symmetric (blue) and asymmetric (red) materials, with dots denoting mobility and bars denoting PLQY.

stacking 6-BTVA, which achieved a high *O* value (1.05), a hole mobility of 9.3 $cm^2\ V^{-1}\ s^{-1}$, and a crystalline PLQY of 30.9 ± 0.53%. The descriptor's general applicability was further confirmed by a linear correlation between positive *O* values and reported PLQYs in known high-mobility emissive crystals. We conclude that the *O* descriptor, combined with an asymmetric design strategy, offers a practical guide for designing and screening high-performance organic crystals with balanced mobility and luminescence.

4 | Experimental Section

4.1 | Computational Details

Density functional theory (DFT) and time-dependent DFT (TD-DFT) calculations were carried out to obtain the equilibrium geometry and excitation energies at S_0 and S_1 states. B3LYP/def2-SVP combined with the polarizable continuum model (PCM) was used to illustrate the photophysical properties of monomers in THF in the Gaussian 16 program package [51]. The energy of the intermolecular CT exciton is much more sensitive to the choice of functional than the energy of the FE. Thus, the use of optimally turned range-separated functional is essential [52, 53]. Reliable prediction of intermolecular CT excitations has been successfully achieved by an optimally turned range-separated functional [54]. The value of ω was turned by minimizing the squared sum of the difference of ionization potential (IP) and the energy of HOMO, and the difference of electronic affinity (EA) and the energy of LUMO:

$$J(\omega)^2 = \sum_{i=0}^{1} \left[\varepsilon_H (N+i) + IP(N+i)\right]^2$$

Three localized diabatic states have been obtained via the Boys localization method [55] using optimally tuned ωB97X-D (ωB97X-D*) with a 6-31G* basis set in the Q-Chem package [56]. The calculations of transfer integrals and exciton couplings *J* were carried out in the PySCF [57] package at the level of ωB97X-D*/6-31G*. The parameters needed in calculating the hole transport mobility are conducted at PW91PW91/6-31G(d) level.

The radiative decay rate constant k_r can be acquired from an integration over the emission spectrum: $k_r(T) = \int \sigma_{em}(\omega, T)d\omega$, where $\sigma_{em}(\omega, T)$ is emission cross section from Fermi Golden Rule (FGR):

$$\sigma_{em}(\omega, T) = \frac{2\omega^3}{3\pi\hbar c^3}|\mu_{fi}|^2 \int_{-\infty}^{+\infty} e^{-i(\omega-\omega_{if})t}\rho_{em}(t, T)\,dt$$

Here μ_{fi} is the electric transition dipole moment between the initial and final electronic states, and $\rho_{em}(t, T) = Z_i^{-1}Tr(e^{-i\tau_f\hat{H}_f}e^{-i\tau_i\hat{H}_i})$ is the Franck–Condon factors at temperature *T* with Z_i is the vibrational partition function of the initial electronic state and $H_{i(f)}$ is the vibrational Hamiltonian for the initial (final) electronic state [58–61].

The nonradiative rate constant between two electronic states within the same spin manifold can be written based on the first-order perturbation theory as:

$$k_{nr} = \frac{1}{\hbar^2}\sum_{kl} R_{kl}\int_{-\infty}^{+\infty} dt e^{i\omega_{if}t}\rho_{fi,kl}^{ic}(t, T)$$

where $R_{kl} = \langle\Phi_f|\hat{P}_{fk}|\Phi_i\rangle\langle\Phi_i|\hat{P}_{fl}|\Phi_f\rangle$ is the nonadiabatic electronic coupling matrix element between electronic states Φ_f and Φ_i and $P_{l(k)}$ is the nuclear momentum operator for the *l(k)*-th vibrational normal mode and $\rho_{fi,kl}^{ic}(t, T) = Z_i^{-1}Tr[\hat{P}_{fk}e^{-i\tau_f\hat{H}_f}\hat{P}_{fl}e^{-i\tau_i\hat{H}_i}]$ [58–61].

Under the hopping regime, the charger transfer rate using the quantum nuclear tunneling can be expressed as [60–63]:

$$k = \frac{V^2}{\hbar}$$
$$\int_{-\infty}^{\infty} dt \times exp\left\{i\omega t - \sum_j S_j\left[(2n_j+1) - n_j e^{-i\omega_j t} - (n_j+1)e^{i\omega_j t}\right]\right\}$$

where ω_j, S_j, and $n_j = 1/[exp(\omega_j/k_BT) - 1]$ are intramolecular vibration frequency, the corresponding Huang–Rhys factor and occupation number for the *j*-th vibrational mode, respectively. The *V* and ω are the transfer integral between two interaction molecules and their energy difference. The carrier mobility can

be obtained via the Einstein relation:

$$\mu = \frac{eD}{(k_B T)}$$

where D can be obtained by:

$$D = \frac{1}{2n} d \left\langle l(t)^2 \right\rangle / dt$$

where n is the spatial dimension ($n = 3$ in a crystal), $l(t)$ is the distance of the carrier's diffusion. The kinetic Monte Carlo (KMC) method is performed to simulate the stochastic process of charge diffusion. The radiative rate constant, nonradiative rate constant, and mobility calculations are performed by using our home-built MOMAP software.

4.2 | Preparation of Single Crystal Samples

High-quality single crystals of 6-BTA, 6-BTVA, 6-BTEA, 2-PhVA, and DPVAnt were prepared via PVT method, in which 20 sccm argon was used as carrier gas, and the heating temperatures were set as 145°C, 160°C, 155°C, 120°C, and 200°C, respectively; hexagonal and rhombic crystals could be obtained at the downstream lower temperature zone with growth temperature of about 50°C–60°C, where the quartz plate was placed.

4.3 | PLQY Study

Photoluminescence spectra were recorded on a PerkinElmer LS 55 spectrofluorometer. For solid-state samples, LabSphere, FluoroMax-4, HORIBA JobinYvon, and the PLQY software package were used. The PLQY was measured using the integrating sphere in combination with a commercial fluorimeter. PLQYs of 49.0%, 84.0%, 30.0%, 67.0%, and 60.0% were obtained for 2-PhVA, DPVAnt, 6-BTA, 6-BTVA, and 6-BTEA in dilute THF solutions (concentration of 10^{-6} M), respectively. Values of (81.5 ± 5.52)%, (9.3 ± 0.28)%, (30.9 ± 0.53)%, (16.1 ± 3.02)%, and (8.0 ± 1.05)% were obtained for single crystals (grown on a circular quartz plate with a diameter of 1 cm), and the mean values with standard deviation were obtained based on 5 samples for 2-PhVA, 6-BTA, and 6-BTVA, and 6 samples for 6-BTEA and DPVAnt, respectively.

[CCDC 2202302, 2202306, 2202307 contain the supplementary crystallographic data for this paper. These data can be obtained free of charge from The Cambridge Crystallographic Data Centre via www.ccdc.cam.ac.uk/data_request/cif.]

Acknowledgments

This work was supported by the National Natural Science Foundation of China (T2225028, 22475219, 12204167, 22325305, T2350009, 52203210, and 22003030), the Chinese Academy of Sciences (Hundred Talents Plan, Youth Innovation Promotion Association, the Strategic Priority Research Program of Sciences [XDB0520200] and Young Scientists in Basic Research [YSBR-053]), and the Guangdong Provincial Natural Science Foundation (2024A1515011185). Jie Liu, Qi Sun, and Yanjun Shi contributed equally to this work.

Conflicts of Interest

The authors declare no conflicts of interest.

References

1. A. Hepp, H. Heil, W. Weise, M. Ahles, R. Schmechel, and H. von Seggern, "Light-Emitting Field-Effect Transistor Based on a Tetracene Thin Film," *Physical Review Letters* 91 (2003): 157406.

2. J. Zaumseil, C. L. Donley, J.-S. Kim, R. H. Friend, and H. Sirringhaus, "Efficient Top-Gate, Ambipolar, Light-Emitting Field-Effect Transistors Based on a Green-Light-Emitting Polyfluorene," *Advanced Materials* 18 (2006): 2708–2712.

3. R. Capelli, S. Toffanin, G. Generali, H. Usta, A. Facchetti, and M. Muccini, "Organic Light-Emitting Transistors With an Efficiency That Outperforms the Equivalent Light-Emitting Diodes," *Nature Materials* 9 (2010): 496–503.

4. M. A. McCarthy, B. Liu, E. P. Donoghue, et al., "Low-Voltage, Low-Power, Organic Light-Emitting Transistors for Active Matrix Displays," *Science* 332 (2011): 570–573.

5. Z. Y. Xie, D. Liu, C. Gao, H. L. Dong, and W. P. Hu, "High-Mobility Emissive Organic Semiconductors: An Emerging Class of Multifunctional Materials," *Nature Reviews Materials* 9 (2024): 837–839.

6. H. C. Liu, Z. C. Xu, J. Zhang, et al., "Integrating Strong Luminescence and High Mobility in Organic Single Crystals of Covalent Pyrene Dimers," *Advanced Materials* 37 (2025): 2419981.

7. J. Deng, Z. Zhang, P. Sang, et al., "Organic Single-Crystal Light-Emitting Transistors With External Quantum Efficiency Over 20%," *Aggregate* 4 (2023): e313.

8. S. Ma, S. Du, G. Pan, S. Dai, B. Xu, and W. Tian, "Organic Molecular Aggregates: From Aggregation Structure to Emission Property," *Aggregate* 2 (2021): e96.

9. P.-Y. Gu, Z. Wang, G. Liu, et al., "Synthesis, Full Characterization, and Field Effect Transistor Behavior of a Stable Pyrene-Fused N-Heteroacene With Twelve Linearly Annulated Six-Membered Rings," *Chemistry of Materials* 29 (2017): 4172–4175.

10. M. Hosseinnezhad, S. Nasiri, V. Nutalapati, K. Gharanjig, and A. M. Arabi, "A Review of the Application of Organic Dyes Based on Naphthalimide in Optical and Electrical Devices," *Progress in Color, Colorants and Coatings* 17 (2024): 417–433.

11. P.-Y. Gu, Y. Zhao, J.-H. He, et al., "Synthesis, Physical Properties, and Light-Emitting Diode Performance of Phenazine-Based Derivatives With Three, Five, and Nine Fused Six-Membered Rings," *Journal of Organic Chemistry* 80 (2015): 3030–3035.

12. F. Cicoira, C. Santato, A. Dadvand, et al., "Environmentally Stable Light Emitting Field Effect Transistors Based on 2-(4-Pentylstyryl)Tetracene," *Journal of Materials Chemistry* 18 (2008): 158–161.

13. T. Yamao, Y. Shimizu, K. Terasaki, and S. Hotta, "Organic Light-Emitting Field-Effect Transistors Operated by Alternating-Current Gate Voltages," *Advanced Materials* 20 (2008): 4109–4112.

14. E. J. Feldmeier, M. Schidleja, C. Melzer, and H. von Seggern, "A Color-Tuneable Organic Light-Emitting Transistor," *Advanced Materials* 22 (2010): 3568–3572.

15. X. H. Liu, I. Wallmann, H. Boudinov, et al., "AC-Biased Organic Light-Emitting Field-Effect Transistors From Naphthyl End-Capped Oligothiophenes," *Organic Electronics* 11 (2010): 1096–1102.

16. S. Hotta and T. Yamao, "The Thiophene/Phenylene Co-Oligomers: Exotic Molecular Semiconductors Integrating High-Performance Electronic and Optical Functionalities," *Journal of Materials Chemistry* 21 (2011): 1295–1304.

17. S. Hotta, T. Yamao, S. Z. Bisri, T. Takenobu, and Y. Iwasa, "Organic Single-Crystal Light-Emitting Field-Effect Transistors," *Journal of Materials Chemistry C* 2 (2014): 965–980.

18. J. Deng, Y. Xu, L. Liu, et al., "An Ambipolar Organic Field-Effect Transistor Based on an AIE-Active Single Crystal With a High Mobility Level of 2.0 $cm^2 V^{-1} s^{-1}$," *Chemical Communications* 52 (2016): 2370–2373.

19. Y. Wan, J. Deng, W. Wu, et al., "Efficient Organic Light-Emitting Transistors Based on High-Quality Ambipolar Single Crystals," *ACS Applied Materials & Interfaces* 12 (2020): 43976–43983.

20. J. Tao, Z. Liu, D. Liu, et al., "High Carrier Mobility and Strong Fluorescence Emission: Toward Highly Sensitive Single-Crystal Organic Phototransistors," *Aggregate* 4 (2023): e269.

21. A. Dadvand, A. G. Moiseev, K. Sawabe, et al., "Maximizing Field-Effect Mobility and Solid-State Luminescence in Organic Semiconductors," *Angewandte Chemie International Edition* 51 (2012): 3837–3841.

22. A. Dadvand, W. H. Sun, A. G. Moiseev, et al., "1,5-, 2,6- and 9,10-Distyrylanthracenes as Luminescent Organic Semiconductors," *Journal of Materials Chemistry C* 1 (2013): 2817–2825.

23. J. Li, J. Liu, Y. G. Zhen, et al., "Naphthyl Substituted Anthracene Combining Charge Transport With Light Emission," *Journal of Materials Chemistry C* 3 (2015): 10695–10698.

24. J. Liu, H. Zhang, H. Dong, et al., "High Mobility Emissive Organic Semiconductor," *Nature Communications* 6 (2015): 10032.

25. M. Chen, Y. Zhao, L. Yan, et al., "A Unique Blend of 2-Fluorenyl-2-Anthracene and 2-Anthryl-2-Anthracence Showing White Emission and High Charge Mobility," *Angewandte Chemie International Edition* 56 (2017): 722–727.

26. J. Li, K. Zhou, J. Liu, et al., "Aromatic Extension at 2,6-Positions of Anthracene Toward an Elegant Strategy for Organic Semiconductors With Efficient Charge Transport and Strong Solid State Emission," *Journal of the American Chemical Society* 139 (2017): 17261–17264.

27. J. Liu, J. Liu, Z. Zhang, et al., "Enhancing Field-Effect Mobility and Maintaining Solid-State Emission by Incorporating 2,6-Diphenyl Substitution to 9,10-Bis(Phenylethynyl)Anthracene," *Journal of Materials Chemistry C* 5 (2017): 2519–2523.

28. Z. Qin, H. Gao, J. Liu, et al., "High-Efficiency Single-Component Organic Light-Emitting Transistors," *Advanced Materials* 31 (2019): 1903175.

29. L. Zheng, J. Li, K. Zhou, et al., "Molecular-Scale Integrated Multi-Functions for Organic Light-Emitting Transistors," *Nano Research* 13 (2020): 1976–1981.

30. Z. Qin, H. Gao, H. Dong, and W. Hu, "Organic Light-Emitting Transistors Entering a New Development Stage," *Advanced Materials* 33 (2021): 2007149.

31. J. Li, Z. Qin, Y. Sun, et al., "Regulating Crystal Packing by Terminal Tert-Butylation for Enhanced Solid-State Emission and Efficacious Charge Transport in an Anthracene-Based Molecular Crystal," *Angewandte Chemie International Edition* 61 (2022): e202206825.

32. P. Wang, C. Gao, Z. J. Ni, et al., "Quinoline Substituted Anthracene Isomers: A Case Study for Simultaneously Optimizing High Mobility and Strong Luminescence in Herringbone-Packed Organic Semiconductors," *Angewandte Chemie International Edition* 64 (2025): e202419213.

33. Q. Sun, J. Ren, T. Jiang, Q. Peng, Q. Ou, and Z. Shuai, "Intermolecular Charge-Transfer-Induced Strong Optical Emission From Herringbone H-Aggregates," *Nano Letters* 21 (2021): 5394–5400.

34. Q. Sun, T. Jiang, Q. Ou, Q. Peng, and Z. Shuai, "Influence of Intermolecular Packing on Light Emitting Efficiency and Carrier-Mobility of Organic Semiconductors: Theoretical Descriptor for Molecular Design," *Advanced Optical Materials* 11 (2023): 2202621.

35. N. J. Hestand and F. C. Spano, "Molecular Aggregate Photophysics Beyond the Kasha Model: Novel Design Principles for Organic Materials," *Accounts of Chemical Research* 50 (2017): 341–350.

36. N. J. Hestand and F. C. Spano, "Expanded Theory of H- and J-Molecular Aggregates: The Effects of Vibronic Coupling and Intermolecular Charge Transfer," *Chemical Reviews* 118 (2018): 7069–7163.

37. L. Jiang, W. Hu, Z. Wei, W. Xu, and H. Meng, "High-Performance Organic Single-Crystal Transistors and Digital Inverters of an Anthracene Derivative," *Advanced Materials* 21 (2009): 3649–3653.

38. F. Qiu, Y. Dong, J. Liu, et al., "Asymmetric Organic Semiconductors for High Performance Single Crystalline Field-Effect Transistors With Low Activation Energy," *Journal of Materials Chemistry C* 8 (2020): 6006–6012.

39. R. A. Laudise, C. Kloc, P. G. Simpkins, and T. Siegrist, "Physical Vapor Growth of Organic Semiconductors," *Journal of Crystal Growth* 187 (1998): 449–454.

40. J. Gierschner, J. Shi, B. Milián-Medina, D. Roca-Sanjuán, S. Varghese, and S. Park, "Luminescence in Crystalline Organic Materials: From Molecules to Molecular Solids," *Advanced Optical Materials* 9 (2021): 2002251.

41. L. Tu, Y. Xie, Z. Li, and B. Tang, "Aggregation-Induced Emission: Red and Near-Infrared Organic Light-Emitting Diodes," *SmartMat* 2 (2021): 326–346.

42. L. Sebastian, G. Weiser, G. Peter, and H. Bässler, "Charge-Transfer Transitions in Crystalline Anthracene and Their Role in Photoconductivity," *Chemical Physics* 75 (1983): 103–114.

43. Y. Ishino, K. Miyata, T. Sugimoto, et al., "Ultrafast Exciton Dynamics in Dinaphtho[2,3-b:2′3′-f]Thieno[3,2-b]-Thiophene Thin Films," *Physical Chemistry Chemical Physics* 16 (2014): 7501–7512.

44. H. Yamagata, C. M. Pochas, and F. C. Spano, "Designing J- and H-Aggregates Through Wave Function Overlap Engineering: Applications to Poly(3-Hexylthiophene)," *Journal of Physical Chemistry B* 116 (2012): 14494–14503.

45. Q. Peng, Y. Yi, Z. Shuai, and J. Shao, "Toward Quantitative Prediction of Molecular Fluorescence Quantum Efficiency: Role of Duschinsky Rotation," *Journal of the American Chemical Society* 129 (2007): 9333–9339.

46. Z. Shuai, D. Wang, Q. Peng, and H. Geng, "Computational Evaluation of Optoelectronic Properties for Organic/Carbon Materials," *Accounts of Chemical Research* 47 (2014): 3301–3309.

47. G. Nan, X. Yang, L. Wang, Z. Shuai, and Y. Zhao, "Nuclear Tunneling Effects of Charge Transport in Rubrene, Tetracene, and Pentacene," *Physical Review B* 79 (2009): 115203.

48. Q. Tang, Y. Tong, H. Li, et al., "High-Performance Air-Stable Bipolar Field-Effect Transistors of Organic Single-Crystalline Ribbons With an Air-Gap Dielectric," *Advanced Materials* 20 (2008): 1511–1515.

49. H. H. Choi, K. Cho, C. D. Frisbie, H. Sirringhaus, and V. Podzorov, "Critical Assessment of Charge Mobility Extraction in FETs," *Nature Materials* 17 (2018): 2–7.

50. Y. Xu, H. Sun, A. Liu, et al., "Essential Effects on the Mobility Extraction Reliability for Organic Transistors," *Advanced Functional Materials* 28 (2018): 1803907.

51. M. J. Frisch, G. W. Trucks, H. B. Schlegel, et al. Gaussian 16, Revision B.01. Gaussian, Inc., Wallingford CT, 2016.

52. R. Baer, E. Livshits, and U. Salzner, "Tuned Range-Separated Hybrids in Density Functional Theory," *Annual Review of Physical Chemistry* 61 (2010): 85–109.

53. L. Kronik, T. Stein, S. Refaely-Abramson, and R. Baer, "Excitation Gaps of Finite-Sized Systems From Optimally Tuned Range-Separated Hybrid Functionals," *Journal of Chemical Theory and Computation* 8 (2012): 1515–1531.

54. T. Stein, L. Kronik, and R. Baer, "Reliable Prediction of Charge Transfer Excitations in Molecular Complexes Using Time-Dependent Density Functional Theory," *Journal of the American Chemical Society* 131 (2009): 2818–2820.

55. J. E. Subotnik, S. Yeganeh, R. J. Cave, and M. A. Ratner, "Constructing Diabatic States From Adiabatic States: Extending Generalized Mulliken–Hush to Multiple Charge Centers With Boys Localization," *Journal of Chemical Physics* 129 (2008): 244101.

56. Y. Shao, Z. Gan, E. Epifanovsky, et al., "Advances in Molecular Quantum Chemistry Contained in the Q-Chem 4 Program Package," *Molecular Physics* 113 (2015): 184–215.

57. Q. Sun, T. C. Berkelbach, N. S. Blunt, et al., "PySCF: The Python-Based Simulations of Chemistry Framework," *Wiley Interdisciplinary Reviews: Computational Molecular Science* 8 (2018): e1340.

58. Q. Peng, Y. Yi, Z. Shuai, and J. Shao, "Toward Quantitative Prediction of Molecular Fluorescence Quantum Efficiency: Role of Duschinsky Rotation," *Journal of the American Chemical Society* 129 (2007): 9333–9339.

59. Y. Niu, Q. Peng, and Z. Shuai, "Promoting-Mode Free Formalism for Excited State Radiationless Decay Process With Duschinsky Rotation Effect," *Science in China, Series B: Chemistry* 51 (2008): 1153–1158.

60. Y. Niu, W. Li, Q. Peng, et al., "MOlecular MAterials Property Prediction Package (MOMAP) 1.0: A Software Package for Predicting the Luminescent Properties and Mobility of Organic Functional Materials," *Molecular Physics* 116 (2018): 1078–1090.

61. Z. Shuai, "Thermal Vibration Correlation Function Formalism for Molecular Excited State Decay Rates," *Chinese Journal of Chemistry* 38 (2020): 1223–1232.

62. G. Nan, X. Yang, L. Wang, Z. Shuai, and Y. Zhao, "Nuclear Tunneling Effects of Charge Transport in Rubrene, Tetracene, and Pentacene," *Physical Review B* 79 (2009): 115203.

63. Z. Shuai, D. Wang, Q. Peng, and H. Geng, "Computational Evaluation of Optoelectronic Properties for Organic/Carbon Materials," *Accounts of Chemical Research* 47 (2014): 3301–3309.

Supporting Information

Additional supporting information can be found online in the Supporting Information section.

Supporting Information file 1: agt270224-sup-0001-SuppMat.docx